materials proceedings

MDPI

Proceedings Paper

Characterizing Hydroxyapatite Deposited from Solution onto Novel Substrates in Terms of Growth Mechanism and Physical Chemical Properties †

Bríd Murphy [1,2,*], Jhonattan Baez [1,2] and M. A. Morris [1,2]

[1] Advanced Materials & Bioengineering Research Centre (AMBER), Trinity College Dublin, Dublin 2, Ireland; email1@gmail.com (J.B.); email2@gmail.com (M.A.M.)
[2] School of Chemistry, Trinity College Dublin, Dublin 2, Ireland
* Correspondence: murphb52@tcd.ie
† Presented at the 4th International Online Conference on Nanomaterials, 5–19 May 2023; Available online: https://iocn2023.sciforum.net.

Abstract: Bulk titanium or CoCr are the most common metal for orthopedic implants but there are significant advantages in alternative substrates. Research in the last decade has focused on various alternatives, however these materials are hindered by the adhesion of a hydroxyapatite layer to non-bulk metal parts. Demonstrated in this work is the ability to grow hydroxyapatite on surfaces other than bulk metallic parts through process and characterisation of coating properties. Here, hydroxyapatite (HA) is grown from saturated solution onto thin titanium films and silicon substrates. Its efficacy is shown to be dependent on substrate roughness. The mechanism of the hydroxyapatite growth is investigated in terms of initial attachment and morphological development using SEM analysis. Characterisation of hydroxyapatite layers by XRD demonstrate how the hydroxyapatite forms from amorphous phases to preferential crystal growth along the [002] direction and TEM imagery confirms specific d-spacings. SEM-EDX and FTIR show adherence to known HA phases through elemental atomic weight percentages and bond assignment. All data is collated and reviewed through the lens of different substrates which suggest that once hydroxyapatite seeds it grows identically regardless of substrate.

Keywords: hydroxyapatite; growth mechanism; characterisation

Citation: Murphy, B.; Baez, J.; Morris, M.A. Characterizing Hydroxyapatite Deposited from Solution onto Novel Substrates in Terms of Growth Mechanism and Physical Chemical Properties. *Mater. Proc.* **2023**, *14*, x. https://doi.org/10.3390/xxxxx
Published: 5 May 2023

1. Introduction

The most common bulk material for knee or hip replacements are chromium-cobalt or titanium alloys due to their mechanical strength and bio-inertness [1,2]. Whilst a common metal for orthopedic implants, there are concerns surrounding titanium's use. Disadvantages of titanium parts include surface propagated cracks, titanium leeching, patient allergies, requirement to add other metals to the titania and a problematic difference between the Young's Modulus of titanium and natural bone [3–9].

Research in the last decade has focused on alternatives to titanium alloys. Polymers have considerable potential in orthopedic implants due to their mechanical properties and biocompatibility [10,11]. Experiments on epoxy coated bamboo fibres found that it had potential as an implant material which would incur lower aseptic loosening post joint replacement due to the fact that its stiffness was close to that of natural bone [12]. Materials for orthopedic parts are hindered by need to add composites or nanomaterials to improve the adhesion of an osteoinductive hydroxyapatite (HA) layer [13,14]. Reviews have called for the need for solution-based HA deposition which contains polymeric particles to be a gateway to implementing polymeric based implants [15].

This work presented in this paper demonstrates the deposition of HA on alternative substrates which would enable effective orthopedic implants of other materials. A novel method of solution deposition whereby phase, porosity and coating integrity are matched to existing HA properties is employed. Titanium coupons (Ti Coupons) are used to model standard orthopedic parts. Novel substrates take the form of planar silicon and titanium thin films and are used to investigate the HA films formed on different surfaces. The data presented regarding titanium thin films shows that HA can be deposited onto a <100 nm thick Ti film without the need for bulk titanium, paving the way for alternative substrates.

2. Materials and Methods

All materials and reagents were used as received. Monobasic potassium phosphate (KH_2PO_4) United States pharmacopeia (USP) reference standard, Honeywell Fluka hydrochloric (HCl) acid solution 6M, Tris(hydroxymethyl)-aminomethane (TRIS) ACS reagent, 99.8% sodium chloride (NaCl) BioXtra, 99.5% calcium nitrate tetrahydrate ($Ca(NO_3)_2.4H_2O$) ACS reagent, all from Sigma Aldrich. KH_2PO_4, TRIS and NaCl were mixed in deionized water (DIW) to yield a supersaturated phosphate solution. HCl was added to added to increase solubility stability and prevent precipitation. $Ca(NO_3)_2.4H_2O$ was mixed with DIW to yield a supersaturated calcium solution. For deposition, the supersaturated solutions were combined before dilution by a factor of 5–10 and warming to 40–50 °C. The mixture was then agitated in a reaction vessel. Four inch silicon wafers were used as received and a subset of these underwent e-beam evaporation-deposition (Temescal FC-2000) to generate 100 nm thin titanium films. Titanium coupons of Ti-6Al-4V alloy were also used. All substrates were submerged in hot basic solutions to increase roughness and foster a more negatively charged surface to which calcium ions can attach [16,17]. Substrates were placed in the reaction vessel for deposition then removed and rinsed with DIW, this process was repeated several times with fresh solutions to grow a coherent layer of HA at the solution-substrate interface.

Atomic Force Microscopy (AFM) was performed using an aXE-7, Park Systems AFM non-contact cantilevers. Scanning Electron Microscopy (SEM) data were collected using a Carl Zeiss Ultra Microscope equipped with an in-Lens detector. An accelerating voltage of 5 to 10 kV was used. Energy-dispersive X-ray spectroscopy (EDX) spectra were acquired at 15 kV on an Oxford Inca EDX detector. X-ray Diffraction (XRD) patterns were acquired using a Bruker Advance Powder Diffractometer (Cu-Kα radiation with $\lambda = 1.5406$ Å, operating voltage of 40 kV and current of 40 mA). Measurements were performed in the 2θ range from 10° to 60° with steps of 0.004°. Transmission Electron Microscopy (TEM) was performed on FEI Titan 80–300 microscope, lamellae for TEM cross-section images were prepared on a Zeiss AURIGA Focused Ion Beam (FIB), accelerating voltages of 5–30 kV and ion beam currents of 50 pA–2 nA. Fourier-transform infrared spectroscopy (FTIR) spectra were obtained using Perkin Elmer's Spotlight 200i benchtop device with Attenuated Total Reflectance (ATR, 4000–500 cm^{-1}, 8 scans, and 4 cm^{-1} resolution diamond crystal).

3. Results

Post activation of substrates, AFM was performed and XEI software was used to calculate roughness values in terms of average roughness (Ra) and peak to valley roughness (RPV) in nanometers for each substrate. The Ra of the novel substrates was <100 nm with the RPV being 125–150 nm albeit lower than the titanium coupons, the roughness was in the same order of magnitude, Figure 1(1).

It was possible to see the effect of this roughness and surface activation after HA deposition run whereby SEM topography had lighter areas of mineral deposits, Figure 1(2a–2c). All three substates generated initial calcium attachment in discrete areas where there were surface groups for bonding. From this initial nucleation heterogeneous growth of needle-like cobweb structure emerged as phosphate groups bonded to the calcium and

wider surface coverage was achieved identically for all three substrates, Figure 1(2a–2c). To delve deeper into the growth mechanism throughout HA deposition runs, XRD patterns were recorded after 2, 4 and 6 process runs, Figure 1(3). Both Ti thin films and silicon had substrate peaks around 33° which diminished as the HA layer grew on the surface Figure 1(3a). These XRD diffractograms showed that the first detection of mineral growth was characteristic HA planes (HA) such as [211], [112] and [310] around 32° but as the process continued the mineral formed was calcium deficient HA (CDHA) indicated by the [002] plane at 26° [18–20]. After 2 process runs the Ti thin film parts showed predominant sharp peaks of HA but the silicon part did not show these until after 4 process runs, implying slower and less mineral growth for silicon Figure 1(3b,3c). The Ti thin film samples followed the growth pattern of a typical titanium part through emergence of CDHA and HA characteristic peaks at given stages in the deposition. The XRD study implied that (i) silicon had some CDHA phase but the least counts therefore the least material and (ii) that the Ti thin film had a lower quantity of same phases as the Ti Coupon.

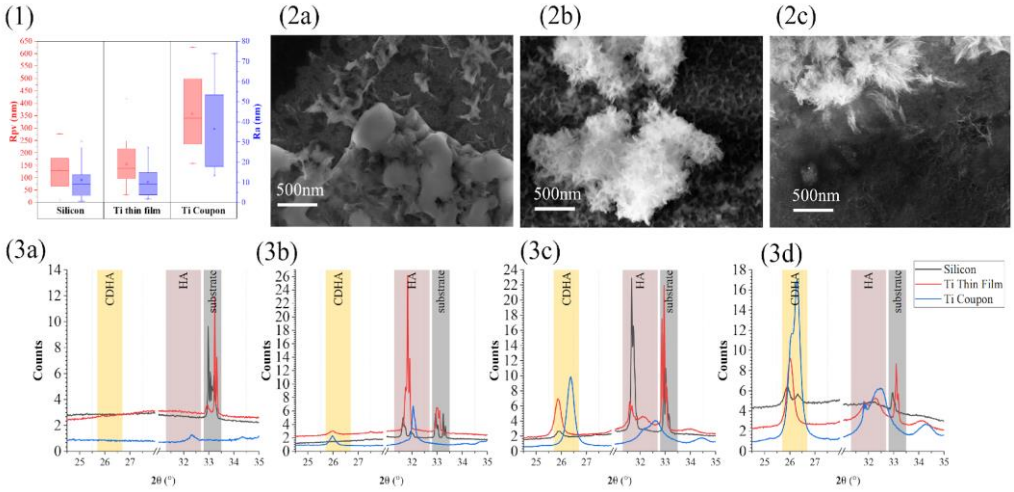

Figure 1. (**1**) The average roughness (Ra) and peak-to-valley (RPV) roughness of the three substrates post activation as measured by Atomic Force Microscopy, (**2**) Scanning Electron Microscopy images taken at 5 kv using inLens detector of samples after the first hydroxyapatite deposition run, (**a**): silicon substrate, (**b**): titanium thin film substrate and (**c**): titanium coupon part. (**3**) X-ray diffraction patterns in terms of counts per second versus diffraction angle of 2θ collected for all three substrates silicon (grey line), Ti thin film (red line) and Ti coupon (blue line), (**a**): post activation prior to any HA deposition, (**b**): post 2 HA deposition runs, (**c**): post 4 HA deposition runs and (**d**): post 6 HA deposition runs.

FIB lamellae were cut through HA films deposited on all three substrate types and subsequent TEM cross-sectional analysis allowed for film thickness measurements. Silicon HA coating measured roughly 1.5 µm, Ti thin films HA coating roughly 5µm and Ti coupon parts' HA coating roughly 6–7 µm in thickness, Figure 2(4a–4c). TEM imagery showed HA with clear layers from the deposition cycles and pockets differing crystal orientations within an amorphous matrix, Figure 2(4d–4f). High resolution TEM images showed ordered lattice fringes for all three substrates and under analysis these d-spacing were comparable to the XRD data peaks (CDHA of 0.34 nm and Pure HA 0.274–0.28 nm) Figure 2(4g–4i).

Further chemical analysis of the HA layers was carried out on samples post full deposition. From FTIR it is evident that silicon substrate had the strongest indication of absorbed water in the HA layer, Figure 2(5a). All substrates had strong vibrational peaks within the known phosphate region of 700 to 1300 cm^{-1}, Figure 2(5b) [21,22]. All substrates demonstrated a matching ratio between the largest peak for $v^3 PO_4^{3-}$ and shoulder peak of

v^1 PO_4^{3-}. Compared to the titanium samples the silicon samples were showing more absorbance of HPO_4^{2-} in agreement with the XRD data. Only Ti coupons samples had a shoulder peak for pure HA. SEM analysis of the HA films post deposition unveiled good coating integrity and similar morphology for both Ti samples, but the silicon samples had less repeatable porosity and interconnectivity, Figure 2(8a–8c). The EDX analysis of these areas supported calculation of the calcium to phosphate ratio (Ca:P) and oxygen atomic percentage (O at%) of these HA films, Figure 2(6a,6b). Silicon has the lowest Ca:P at 1.25 ± 0.12 but the Ti thin film was 1.36 ± 0.14 very close to a Ti coupon at 1.38 ± 0.07, Figure 2(6b).

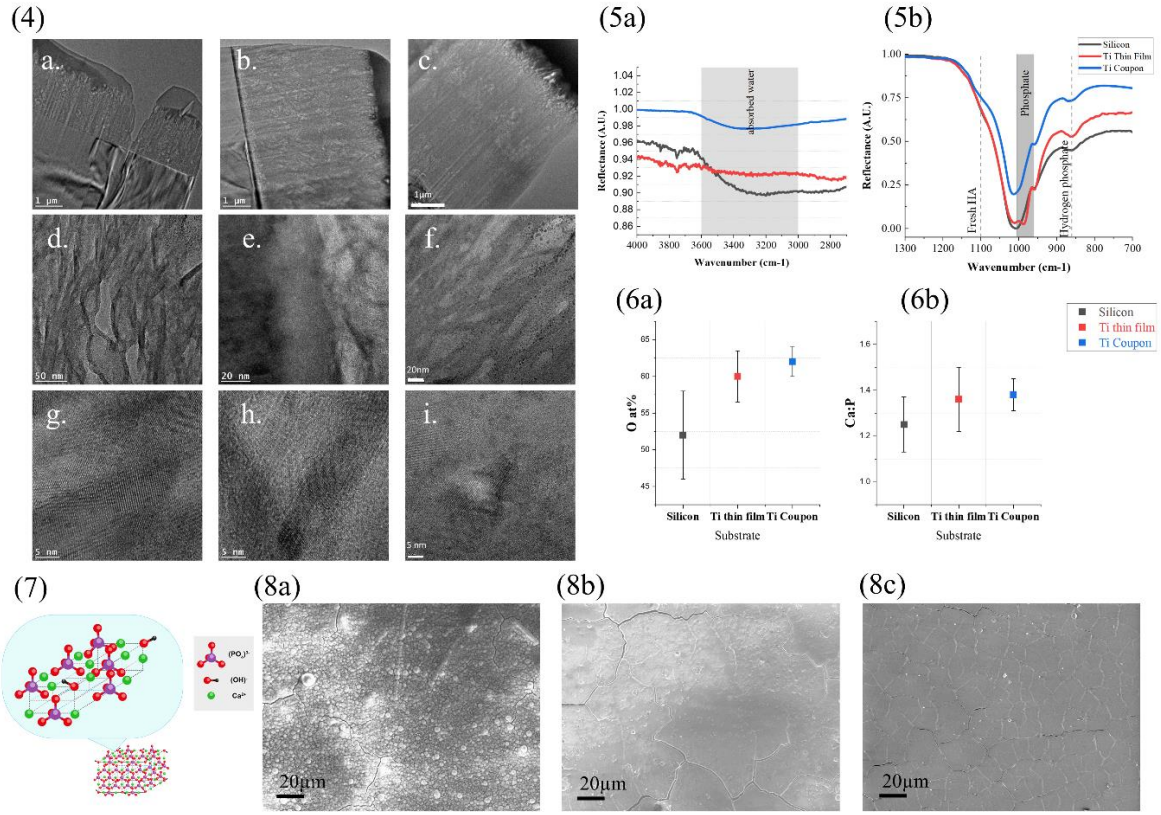

Figure 2. (**4**(**a**–**i**)) Transmission Electron Microscopy cross-sectional images of lamellae cut through HA layers, 1 µm scale, 50 nm scale bar and higher magnification nanometer scale (**a**,**d**,**g**): Cross-section of the HA layer over silicon substrate (**b**,**e**,**h**): Cross-section of the HA layer over Ti thin film substrate (**c**,**f**,**i**): Cross-section of the HA layer over Ti coupon part, (**5**): Fourier Transform infrared spectra (**a**) in the absorbed water region of 4000–2000 cm^{-1} and (**b**) in the phosphate region of 1300–700 cm^{-1} of the full deposited HA layer over all three substrates silicon (grey line), Ti thin film (red line) and Ti coupon (blue line). (**6**) Collated Electron dispersive X-ray data showing mean and error bars for the atomic percentage of (**a**) oxygen (O at%) and (**b**) calcium to phosphorus atomic percentage (Ca:P) found in the HA film deposited over silicon, Ti thin film and Ti coupon parts, (**7**) Crystal structure of hydroxyapatite. For better visualization some atoms have been removed from the diagram; The diagram has been constructed from the literature [23,24] and (**8**) Scanning Electron Microscopy images taken at 5 kv using inLens detector of samples after 6 HA deposition runs, (**a**): silicon substrate, (**b**): Ti thin film substrate and (**c**): titanium coupon part.

The unit cell of pure HA, formula $C_{10}(PO_4)_6(OH)$ has hydroxyl ions at the corners of the planes, and phosphate anions and Ca^{2+} cations forming a hexagonal P63/m space group, see Figure 2(7). Other phases of HA exist, and from the data herein it became clear that HA films formed from this solution deposition process were a combination of phases. Pure HA has a Ca:P of 1.67 and O at% of 34.9%, amorphous calcium phosphate (ACP) $CaxHy(PO_4)z{\cdot}nH_2O$ has a varying Ca:P and O at %, and octacalcium phosphate (OCP)

$Ca_8H_2(PO_4)_6{\cdot}5H_2O$ corresponding to a calcium deficient HA phase which has a Ca:P of 1.33 with an O at% of 39.7%. The Ca:P of all three samples heavily indicated the predominant formation of OCP which supported the XRD observations. Samples in this study had O at% of 52 ± 6% for silicon, 60 ± 3.5% for Ti thin film and 62 ± 2% for Ti coupon, so all three possessed a higher oxygen content than the known phases implying added ACP and hydrogen phosphates but also the present of adsorbed water and oxides around the lattice. Silicon samples were showing the highest O at% again implying the lowest pure HA content.

4. Conclusion

Successful deposition of hydroxyapatite films using a novel colloidal solution deposition process and its efficacy for non-bulk titanium parts was confirmed in this work. AFM analysis showed that although the two novel type substrates were less rough than a typical titanium part, SEM data proved that after the first process run, HA mineral deposits were generated. XRD revealed the pathway by which HA grows within this process for a typical titanium part and that a Ti thin film parts follow this mechanism closely, but silicon has a slower growth mechanism. Through TEM analysis the thickness and crystallinity of layers were compared and while silicon has less material, all three substrates had crystalline pockets within an amorphous matrix. Chemical composition of the film from FTIR and SEM-EDX data showed that all three had ACP and OCP present with little pure HA, but the silicon had higher impurities.

Overall, it has been confirmed that a Ti thin film can support the growth of HA layer matched to a Ti coupon part. This opens possibilities of coating non-bulk metallic orthopedic implants

Author Contributions: Conceptualization, B.M. and M.A.M.; methodology, B.M. and M.A.M.; investigation, B.M. and M.A.M.; writing—original draft preparation, B.M.; writing—review and editing, J.B. and M.A.M., visualization, J.B.; supervision, M.A.M. All authors have read and agreed to the published version of the manuscript.

Funding: This publication has emanated from research supported in part by a research grant from Science Foundation Ireland (SFI) and is co-funded under the European Regional Development Fund under Grant Number 12/RC/2278 and Grant Number 17/RC-PhD/3477. This research has been co-funded by DePuy Synthes (Ireland).

Acknowledgments: We thank Lucie Hankey and Aidan Cloonan, for technical advice and scientific discussions. We thank the AML center and especially Dr Raman Bekarevich for TEM analysis support.

Conflicts of Interest: The authors declare no conflict of interest.

References

1. Dobbs, H.S.; Scales, J.T. Behavior of Commercially Pure Titanium and Ti-318 (Ti-6Al-4V) in Orthopedic Implants. *Titan. Alloy. Surg. Implant.* **1983**, 173–186. https://doi.org/10.1520/STP28942S.
2. Keegan, G.M.; Learmonth, I.D.; Case, C. A Systematic Comparison of the Actual, Potential, and Theoretical Health Effects of Cobalt and Chromium Exposures from Industry and Surgical Implants. *Crit. Rev. Toxicol.* **2008**, *38*, 645–674. https://doi.org/10.1080/10408440701845534.
3. Grupp, T.M.; Weik, T.; Bloemer, W.; Knaebel, H.-P. Modular Titanium Alloy Neck Adapter Failures in Hip Replacement—Failure Mode Analysis and Influence of Implant Material. *BMC Musculoskelet. Disord.* **2010**, *11*, 3. https://doi.org/10.1186/1471-2474-11-3.
4. Siddiqi, A.; Payne, A.G.T.; Silva, R.K.D.; Duncan, W.J. Titanium Allergy: Could It Affect Dental Implant Integration? *Clin. Oral Implant. Res.* **2011**, *22*, 673–680. https://doi.org/10.1111/j.1600-0501.2010.02081.x.
5. Swiatkowska, I.; Martin, N.; Hart, A.J. Blood Titanium Level as a Biomarker of Orthopaedic Implant Wear. *J. Trace Elem. Med. Biol.* **2019**, *53*, 120–128. https://doi.org/10.1016/j.jtemb.2019.02.013.
6. Niinomi, M.; Nakai, M. Titanium-Based Biomaterials for Preventing Stress Shielding between Implant Devices and Bone. *Int. J. Biomater.* **2011**, *2011*, 836587. https://doi.org/10.1155/2011/836587.

7. Shi, Y.D.; Wang, L.N.; Liang, S.X.; Zhou, Q.; Zheng, B. A High Zr-Containing Ti-Based Alloy with Ultralow Young's Modulus and Ultrahigh Strength and Elastic Admissible Strain. *Mater. Sci. Eng. A* **2016**, *674*, 696–700. https://doi.org/10.1016/j.msea.2016.08.038.
8. Tan, M.H.C.; Baghi, A.D.; Ghomashchi, R.; Xiao, W.; Oskouei, R.H. Effect of Niobium Content on the Microstructure and Young's Modulus of Ti-XNb-7Zr Alloys for Medical Implants. *J. Mech. Behav. Biomed. Mater.* **2019**, *99*, 78–85. https://doi.org/10.1016/j.jmbbm.2019.07.014.
9. Nakai, M.; Niinomi, M.; Zhao, X.; Zhao, X. Self-Adjustment of Young's Modulus in Biomedical Titanium Alloys during Orthopaedic Operation. *Mater. Lett.* **2011**, *65*, 688–690. https://doi.org/10.1016/j.matlet.2010.11.006.
10. Abitha, H.; Kavitha, V.; Gomathi, B.; Ramachandran, B. A Recent Investigation on Shape Memory Alloys and Polymers Based Materials on Bio Artificial Implants-Hip and Knee Joint. *Mater. Today Proc.* **2020**, *33*, 4458–4466. https://doi.org/10.1016/j.matpr.2020.07.711.
11. Saad, M.; Akhtar, S.; Srivastava, S. Composite Polymer in Orthopedic Implants: A Review. *Mater. Today Proc.* **2018**, *5*, 20224–20231. https://doi.org/10.1016/j.matpr.2018.06.393.
12. Ismail, N.F.; Shuib, S.; Romli, A.Z.; Saeid, N.H. Epoxy-Coated of Bamboo Fibre Reinforced Polymer Composite for Uncemented Total Hip Replacement (THR) Application. *J. Mech. Eng.* **2020**, *9*, 167–177.
13. Auclair-Daigle, C.; Bureau, M.N.; Legoux, J.-G.; Yahia, L. Bioactive Hydroxyapatite Coatings on Polymer Composites for Orthopedic Implants. *J. Biomed. Mater. Res. Part A* **2005**, *73A*, 398–408. https://doi.org/10.1002/jbm.a.30284.
14. Balasundaram, G.; Webster, T.J. An Overview of Nano-Polymers for Orthopedic Applications. *Macromol. Biosci.* **2007**, *7*, 635–642. https://doi.org/10.1002/mabi.200600270.
15. Andrusova, N.N.; Zhavoronok, E.S.; Legon'kova, O.A.; Goncharova, A.S.; Kedik, S.A. Polymer–Mineral Compounds for Cementless Hip Replacement. *Polym. Sci. Ser. D* **2020**, *13*, 68–72. https://doi.org/10.1134/S1995421220010037.
16. de Andrade, M.C.; Filgueiras, M.R.; Ogasawara, T. Nucleation and Growth of Hydroxyapatite on Titanium Pretreated in NaOH Solution: Experiments and Thermodynamic Explanation. *J. Biomed. Mater. Res.* **1999**, *46*, 441–446. https://doi.org/10.1002/(sici)1097-4636(19990915)46:4<441::aid-jbm1>3.0.co;2-9.
17. Kim, C.; Kendall, M.R.; Miller, M.A.; Long, C.L.; Larson, P.R.; Humphrey, M.B.; Madden, A.S.; Tas, A.C. Comparison of Titanium Soaked in 5 M NaOH or 5 M KOH Solutions. *Mater. Sci. Eng. C Mater. Biol. Appl.* **2013**, *33*, 327–339. https://doi.org/10.1016/j.msec.2012.08.047.
18. Keller, L.; Rey-Fessler, P. Nondestructive Characterization of Hydroxylapatite Coated Dental Implants by XRD Method. In *Characterization and Performance of Calcium Phosphate Coatings for Implants*; Horowitz, E., Parr, J.E., Eds.; ASTM International: Miami, FL, USA, 1992.
19. Ślósarczyk, A.; Paszkiewicz, Z.; Paluszkiewicz, C. FTIR and XRD Evaluation of Carbonated Hydroxyapatite Powders Synthesized by Wet Methods. *J. Mol. Struct.* **2005**, *744–747*, 657–661. https://doi.org/10.1016/j.molstruc.2004.11.078.
20. Chappard, C.; André, G.; Daudon, M.; Bazin, D. Analysis of Hydroxyapatite Crystallites in Subchondral Bone by Fourier Transform Infrared Spectroscopy and Powder Neutron Diffraction Methods. *Comptes Rendus Chim.* **2016**, *19*, 1625–1630. https://doi.org/10.1016/j.crci.2015.03.015.
21. Rehman, I.; Bonfield, W. Characterization of Hydroxyapatite and Carbonated Apatite by Photo Acoustic FTIR Spectroscopy. *J. Mater. Sci. Mater. Med.* **1997**, *8*, 1–4. https://doi.org/10.1023/A:1018570213546.
22. Ślósarczyk, A.; Paluszkiewicz, C.; Gawlicki, M.; Paszkiewicz, Z. The FTIR Spectroscopy and QXRD Studies of Calcium Phosphate Based Materials Produced from the Powder Precursors with Different Ratios. *Ceram. Int.* **1997**, *23*, 297–304. https://doi.org/10.1016/S0272-8842(96)00016-8.
23. Rujitanapanich, S.; Kumpapan, P.; Wanjanoi, P. Synthesis of Hydroxyapatite from Oyster Shell via Precipitation. *Energy Procedia* **2014**, *56*, 112–117. https://doi.org/10.1016/j.egypro.2014.07.138.
24. Pramatarova, L.; Pecheva, E. *Modified Inorganic Surfaces as a Model for Hydroxyapatite Growth*; Trans Tech Publications Limited: Stafa-Zurich, Switzerland, 2006.